ChemComm

COMMUNICATION

View Article Online
View Journal | View Issue

Cite this: *Chem. Commun.*, 2023, **59**, 944

Received 30th August 2022,
Accepted 19th December 2022

DOI: 10.1039/d2cc04810h

rsc.li/chemcomm

Hybrid photocathode based on a Ni molecular catalyst and Sb_2Se_3 for solar H_2 production†

D. Alicia Garcia-Osorio,[a] Thomas P. Shalvey,[a] Liam Banerji,[a] Khezar Saeed,[ab] Gaia Neri,‡[a] Laurie J. Phillips,[a] Oliver S. Hutter,[ac] Carla Casadevall,[d] Daniel Antón-García,[d] Erwin Reisner,[d] Jonathan D Major*[a] and Alexander J Cowan*[a]

We report a H_2 evolving hybrid photocathode based on Sb_2Se_3 and a precious metal free molecular catalyst. Through the use of a high surface area TiO_2 scaffold, we successfully increased the Ni molecular catalyst loading from 7.08 ± 0.43 to 45.76 ± 0.81 nmol cm^{-2}, achieving photocurrents of 1.3 mA cm^{-2} at 0 V *vs.* RHE, which is 81-fold higher than the device without the TiO_2 mesoporous layer.

Photoelectrodes for the production of solar fuels, for example by splitting water to generate H_2 and O_2,[1] have the potential to play a key role in future energy systems. However, advances in both photoanodes for water oxidation[2] and photocathodes for hydrogen evolution (HER) are needed to improve the stability and to lower the cost for industrial scaling, since most long-lasting devices rely on precious metals.[3–5] Sb_2Se_3 has recently gained interest from the photovoltaic (PV) community due to its near-direct band gap of 1.18 eV, a high absorption coefficient across the visible region,[6] and an unusual 1D nanoribbon structure that enables effective charge transport.[7] These properties, combined with improvements in material processability and the use of earth-abundant elements, have led to the suggestion that Sb_2Se_3 could be a viable thin film PV material for use on a global scale.[8] Sb_2Se_3 has also been studied as a photocathode for HER, the conduction band minimum at −0.5 V *vs.* RHE provides enough driving force for producing H_2,[9] and its band gap (E_g) is very close to the optimal calculated for the bottom electrode in dual absorber standalone device for water splitting.[10] Reported solar to hydrogen efficiencies, using state-of-the-art Sb_2Se_3 photocathodes, have now exceeded 10%.[11,12] These photocathodes consist of a Sb_2Se_3/CdS buried junction that is coated with a protective TiO_2 capping layer. The planar TiO_2 is then modified with a HER catalyst like Pt,[13,14] RuO_2,[12,15] and MoS_x.[16] Notably, even with state-of-the-art devices, reductive dissolution of TiO_2 caused by photoelectron accumulation can occur.[11,13] C_{60} between TiO_2 and the H_2-evolution catalyst can alleviate charge accumulation promoting the photoelectron transfer at the TiO_2/Pt interface, but device stabilities are still low.[11,13] Therefore, a need still exists to identify new active photoelectrode/catalysts systems that are able to keep up with the rate of photoelectron generation and to explore how the catalyst/TiO_2 interface can be modified to prevent the generation of high-electron densities. Earth abundant molecular electrocatalysts have not previously been explored on Sb_2Se_3 photocathodes, even though they are an alternative to precious metal electrocatalysts and could potentially offer improved rates of charge transfer at the semiconductor/molecular catalyst interface.[17,18] Here, **NiP** with a $[Ni(P_2^{R'}N_2^{R''})_2]^{2+}$ core ($P_2^{R'}N_2^{R''}$ = bis(1,5-R′-diphospha-3,7-R″-diazacyclooctane)), shown in Fig. 1b, was chosen as model molecular catalyst.[19] The **NiP** catalyst mimics the hydrogenase intramolecular proton transfer to the Ni centre through the pendant amine groups in the second coordination sphere.[20] Furthermore, it can be covalently anchored to TiO_2 by the phosphonic acid groups in the outer coordination sphere, Fig. 1b.[21]

The complete device FTO/Au/Sb_2Se_3/CdS/TiO_2/TiO_2-*meso*/**NiP** is shown in Fig. 1a. Sb_2Se_3 (1.5 μm) was deposited on Au (70 nm) coated fluorine-doped SnO_2-glass (FTO) by a two-step fast-cooling close space sublimation process, which generates a compact preferentially orientated nanoribbon crystal structure that facilitates rapid hole transfer to the Au contact.[7,11,12] Then, a thin sputtered CdS buffer layer (20 nm) was added which forms a Sb_2Se_3 heterojunction with a negligible conduction band offset, thereby allowing efficient charge separation and electron transfer towards TiO_2 (Fig. 1c).[6] In this way, the onset potential and fill factor of the Sb_2Se_3 photocathodes are improved despite the parasitic absorption of photons below $\lambda < 500$ nm in the CdS causing a decrease in the photocurrent.[11,12] After, TiO_2 (100 nm) was sputtered to provide a physical barrier preventing contact between the light absorber

[a] *Stephenson Institute for Renewable Energy, University of Liverpool, L69 7ZF, UK. E-mail: acowan@liverpool.ac.uk*
[b] *Department of Chemistry, Aarhus University, Aarhus C 8000, Denmark*
[c] *Department of Mathematics, Physics and Electrical Engineering, Northumbria University, NE1 8ST, UK*
[d] *Yusuf Hamied Department of Chemistry, University of Cambridge, CB2 1EW, UK*

† Electronic supplementary information (ESI) available. See DOI: https://doi.org/10.1039/d2cc04810h

‡ Current address: Enapter S.R.L, *via* di Lavoria 56/g, 56040 Pisa.

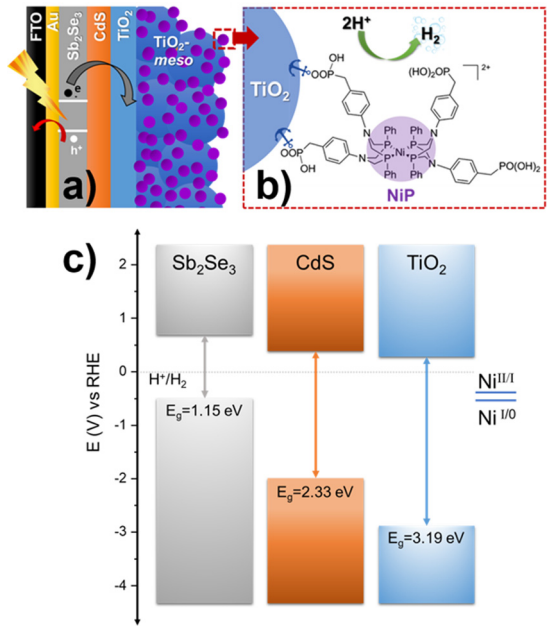

Fig. 1 (a) Schematic diagram of Sb_2Se_3/CdS/TiO_2-*meso*/**NiP** hybrid photocathode. (b) Chemical structure of **NiP** catalyst molecular catalyst, panel a and b are not drawn to scale. (c) Equilibrium band alignment diagram of Sb_2Se_3/CdS/TiO_2 heterojunction based on VBM[11] and E_g measured separately for each layer (Fig. S2.1, ESI†), note that **NiP** redox couple is pH independent.[21]

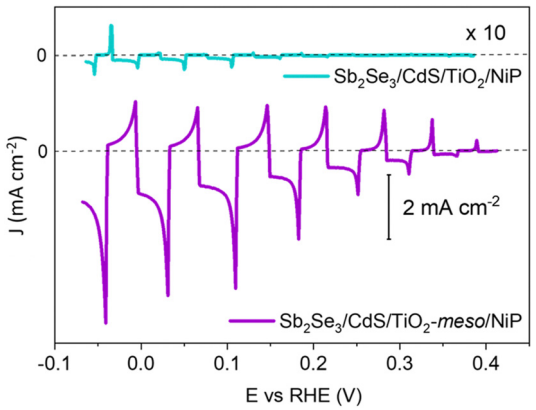

Fig. 2 Chopped light LSV of the hybrid photocathodes Sb_2Se_3/CdS/TiO_2/**NiP** (blue trace) and Sb_2Se_3/CdS/TiO_2-*meso*/**NiP** (purple trace) at 10 mV s^{-1}. The TiO_2-*meso* enables a higher loading of the **NiP** catalysts and increased photocurrents. All experiments were carried out in 0.1 M Na_2SO_4 pH 3 at 100 mW cm^{-2} and $\lambda > 340$ nm.

and the electrolyte.[22] Full details of the synthetic procedures, the device characterisation and SEM images are provided in the ESI,† Fig. S2.1-3.

The molecular catalyst was first immobilized overnight onto the sputtered TiO_2 (without the TiO_2-*meso*) by soaking the photoelectrode in dry methanolic solution (0.5 mM **NiP**),[19,23,24] and from now on labelled as Sb_2Se_3/CdS/TiO_2/**NiP**. It was removed from the soaking solution, thoroughly washed in methanol to remove the non-chemisorbed catalyst and dried under vacuum. **NiP** loadings were determined by stripping the catalyst off using NaOH and then quantified by UV-vis spectroscopy, as shown in Table S1 (ESI†). When **NiP** was attached to the sputtered TiO_2 layer, a loading of 7.08 ± 0.43 nmol cm^{-2} was achieved. All the photoelectrochemical tests were done under 100 mW cm^{-2} illumination (unless otherwise stated) and with $\lambda > 340$ nm in 0.1 M Na_2SO_4 at pH 3. pH 3 was chosen due to past studies that showed **NiP** was most active at this pH.[23,25] Fig. 2 shows a photocurrent of only −16 μA cm^{-2} at 0 V *vs.* RHE, which exceeds only slightly the current in the absence of any catalyst (−3 μA cm^{-2} for Sb_2Se_3/CdS/TiO_2, Fig. S2.4, ESI†). The spikes in the light chopped Linear Sweep Voltammetry (LSV) of Sb_2Se_3/CdS/TiO_2/**NiP** demonstrated that the photoelectrons are not being utilised at a fast-enough rate by the catalyst, instead recombination is dominating.[26]

The low photocurrent of the Sb_2Se_3/CdS/TiO_2/**NiP** electrode is due to the low loading of **NiP** compared with previous devices.[23,24] A common approach to achieve higher catalyst loadings on a photoelectrode is to increase the available surface area for catalyst binding by using a mesoporous TiO_2 layer (TiO_2-*meso*). Typically, following deposition of a TiO_2 nanoparticle-organic binder paste, thermal annealing is carried out in air (~450 °C) to remove the binder and sinter the TiO_2 nanoparticles forming conductive pathways.[26] Sb_2Se_3 is unstable at these temperatures in air,[8] therefore we modified a UV curing approach successfully developed by the Grätzel group for CuO_2/AZO/TiO_2 photocathodes.[27] Following doctor blading of an anatase TiO_2 paste (*av.* particle size 20 nm diameter) the sample was UV cured for 68 h using a 365 nm LED, Fig. S2.5 (ESI†). Note that the Sb_2Se_3/CdS/TiO_2-*meso* also included the sputtered 100 nm TiO_2 layer since it was found to be essential during the UV curing to protect the Sb_2Se_3/CdS. The photocathode was then annealed at lower temperature (350 °C) under N_2 to improve the electrochemical properties of the TiO_2-*meso* layer (Fig. S2.6-7, ESI†) without hindering the light absorber capabilities (Fig. S2.9, ESI†). The TiO_2-*meso* was *ca.* 4–6 μm thick determined by profilometry, the cross-sectional image and energy-dispersive X-ray spectroscopy (EDX) maps are shown Fig. 3a and Fig. S2.10 (ESI†), respectively. Neither the UV curing nor the N_2 annealing alone resulted in a TiO_2-*meso* layer with electrical and mechanical features suitable for a molecular catalyst scaffold (Fig. S2.5 and S2.8, ESI†). The **NiP** immobilization on the TiO_2-*meso* device was carried out using the same experimental protocol as for the planar structure. The resultant Sb_2Se_3/CdS/TiO_2-*meso*/**NiP** photocathode achieved an increased **NiP** loading (45.76 ± 0.81 nmol cm^{-2}), in line with the literature.[24] Top view EDX mapping shows the catalyst is evenly distributed on the photocathode surface (Fig. S2.11, ESI†). X-Ray photoelectron spectroscopy (XPS) analysis of the **NiP** on the Sb_2Se_3/CdS/TiO_2-*meso*/**NiP** electrode is shown in Fig. 3b–d. The energies of the Ni 2p (Fig. 3b, 1/2 at 872.1 eV and 3/4 at 854.6), P 2p (Fig. 3c, 132.6 eV) and N 1s (Fig. 3d, 399.6 eV) peaks are in good agreement with the **NiP** catalyst prior to immobilisation (all the XPS peak positions are shown in Table S2, ESI†).[23–25] The complete Sb_2Se_3/CdS/TiO_2-*meso*/**NiP** photocathode achieves a photocurrent of −1.3 mA cm^{-2} at 0 V *vs.* RHE with an onset potential of *ca.* +0.37 V *vs.* RHE (Fig. 2). The photocurrent for this electrode structure is amongst the highest reported for a **NiP** decorated photocathode, Table S3 (ESI†)

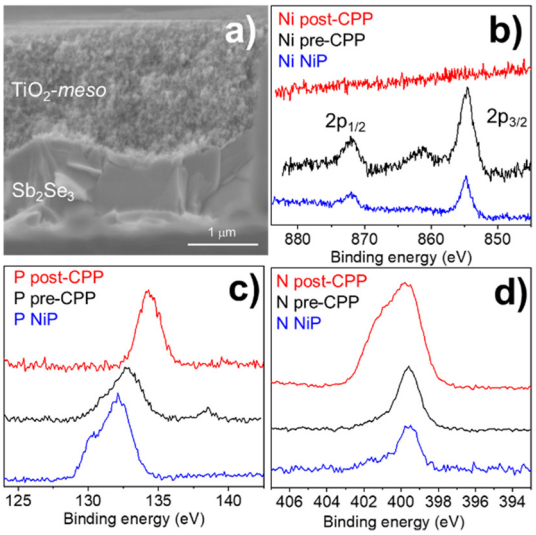

Fig. 3 (a) Cross-sectional SEM image of Sb_2Se_3/CdS/TiO_2-*meso*/**NiP**. (b–d) XPS spectra of **NiP** molecular catalyst (blue trace) after it is immobilized on TiO_2 (pre-CPP,black trace), and after 5 h of CPP test at 0 V *vs.* NHE (post-CPP, red trace) with light intensity of 100 mW cm^{-2} and $\lambda > 340$ nm in 0.1 M Na_2SO_4 at pH 3. (b–d) XPS spectra showing Ni 2p, P 2p and N 1s regions respectively.

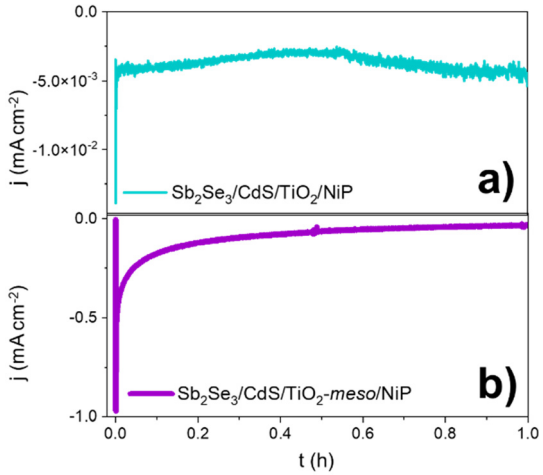

Fig. 4 CPP at 0 V *vs.* RHE of the hybrid photocathodes Sb_2Se_3/CdS/TiO_2/**NiP** (a) and Sb_2Se_3/CdS/TiO_2-*meso*/**NiP** (b) in 0.1 M Na_2SO_4 pH 3 at 100 mW cm^{-2} and $\lambda > 340$ nm.

provides the state-of-the-art hybrid photocathodes for H_2 production. **NiP** has been previously used with a Si/TiO_2-*meso* photocathode to achieve a photocurrent of −0.3 mA cm^{-2} at 0 V *vs.* RHE[24] and −0.6 mA cm^{-2} at 0 V *vs.* RHE for a $La_5Ti_2Cu_{0.9}Ag_{0.1}S_5O_7$/$TiO_2$ photocathode.[23] A control experiment without the catalyst (Sb_2Se_3/CdS/TiO_2-*meso*, Fig. S2.4. ESI†) demonstrates the importance of the **NiP** catalyst, it showed a photocurrent of only −0.12 mA cm^{-2} at 0 V *vs.* RHE. Incident photon to current efficiency (IPCE, Fig. S2.12, ESI†) demonstrates the device is active at wavelengths up to 900 nm (at 0 V *vs.* RHE), in-line with the E_g of Sb_2Se_3.[6,7]

Controlled potential photoelectrolysis (CPP) carried out at 0 V *vs.* RHE assessed the stability of the Sb_2Se_3/CdS/TiO_2-*meso*/**NiP** electrode, results shown in Fig. 4. The H_2 faradaic efficiency after 1 h was 77.5 ± 9.1%, giving a TON_{NiP} of 12.8 ± 2.8. However, the photocurrent decreased significantly in the first hour reaching −40 μA cm^{-2} and by 5 hours, it decreased to only −15 μA cm^{-2} (Fig. S2.13, ESI†). The loss of photoactivity of **NiP** photoelectrodes has previously been attributed to the hydrolysis of the phosphonic anchoring group from the TiO_2.[23,24] XPS analysis of the hybrid photocathode post CPP shows the loss of the Ni^{2+} bands (red trace, Fig. 3b). However, it is clear that both the N 1s and P 2p signals are still present, although significantly shifted. A broadening of the N 1s band has previously been assigned to protonation of the amine in the acidic electrolyte[23] and the shifting of the P band is due to the loss of the metal centre.[28] The XPS results suggest the phosphonate linkage has been retained but the Ni is no longer coordinated to the ligand, in-line with the stability of the phosphonate linkage at pH < 7.[29] Past studies have shown that **NiP** degradation occurs on photocathodes but with a slower decay rate.[23,24]

To explore the mechanism of the hybrid photocathode decay here, we examined the TiO_2-*meso*/**NiP** interface (without Sb_2Se_3/CdS). CPE at −0.24 V *vs.* RHE (Fig. S2.7b, ESI†), shows that following an initial drop in the current in the first 600 s, the electrode maintains a stable current of −0.24 mA cm^{-2} for 1 h suggesting that the TiO_2-*meso*/**NiP** interface is stable at this potential and capable of dealing with low current density. However, the current spikes observed with Sb_2Se_3/CdS/TiO_2-*meso*/**NiP** when the light is turned off in Fig. 2 are typical features of electron accumulation in the TiO_2, suggesting that the **NiP** catalyst was unable to turnover at the rate of photoelectron generation under 100 mW cm^{-2} illumination. Based on the concentration of immobilised **NiP** (45.76 ± 0.81 nmol cm^{-2}), and the highest reported turnover frequency of **NiP** (460 ± 5 h^{-1}),[21] we calculate that the **NiP** on the surface could support a photocurrent of −1.15 mA cm^{-2}. This magnitude of photocurrent is achieved briefly in the LSV, but CPP shows the photocurrent decreases rapidly as the **NiP** catalyst degrades. To assess the photoelectron generation of Sb_2Se_3/CdS/TiO_2-*meso*, we used Pt as co-catalyst (see ESI,† for synthetic details, Fig. S2.14). The Sb_2Se_3/CdS/TiO_2-*meso*/Pt electrode achieved a stable photocurrent of −3 mA cm^{-2} at 0 V *vs.* RHE for 5 hours. It is clear that the rate of photoelectron generation at the Sb_2Se_3/CdS interface greatly exceeds the maximum current density that **NiP** can sustain. The catalytic mechanism of **NiP** is shown in Fig. S2.15 (ESI†),[20] H_2 production occurs following the $Ni^{II/I}$ reduction. Further reduction from Ni^{I} to Ni^{0} can also potentially occur deactivating the catalyst if the rate of photoelectron generation is too high.[30] To explore if limiting the photoelectron generation on the Sb_2Se_3 would be beneficial, experiments at 20 mW cm^{-2} (Fig S2.16 and S17, ESI†) were carried out. Notably, only a small decrease in photocurrent was observed from 1.30 to 0.81 mA cm^{-2} at 0 V *vs.* RHE, and 20% of photocurrent was retained after 1800 s compared with the 11% at 100 mW cm^{-2}.

Past studies using precious metal HER catalysts like Pt on planar TiO_2 coated Sb_2Se_3 photocathodes have noted that

dissolution of TiO_2 can also occur due to photoelectron accumulation.[11,13] The SEM images post-CPP Sb_2Se_3/CdS/TiO_2-*meso*/**NiP** electrodes (tested at 100 mW cm^{-2}) did not show significant change in the morphology of the device (Fig. S2.18, ESI†) despite the demonstration of electron accumulation in the device. XRD analysis of a post-CPP sample only showed the typical peaks of Sb_2Se_3 and TiO_2 (Fig. S2.19, ESI†) and no indication of Sb_2O_3 formation, which has been associated with the deactivation of the Sb_2Se_3 photoelectrodes (Fig. S2.20, ESI†).[12,13] However experiments where Sb_2Se_3/CdS/TiO_2-*meso*/**NiP** underwent (i) LSV and CPP at 0 V *vs.* RHE for 1 h, (ii) removal of any remaining **NiP** by NaOH stripping, and (iii) Pt addition and photoelectrochemical testing showed evidence of partial failure of the sputtered TiO_2 layer due to photoelectron accumulation. Significantly higher dark currents (< -5 mA cm^{-2}, Fig. S2.21, ESI†) and decreased photocurrents were measured compared to a pristine platinized photoelectrode, reinforcing the importance of preventing photoelectron accumulation in the Sb_2Se_3/CdS/TiO_2-*meso*/**NiP** photocathode.

Emergent chalcogenide semiconductors such as Sb_2Se_3 are promising photocathodes due to their ability to achieve a high rate of photoelectron generation but they suffer from thermal instability limiting processing opportunities. Furthermore, Sb_2Se_3 interfaces need to be protected by metal oxide capping layers where corrosion could occur due to photoelectron accumulation. To prevent electron accumulation research has focused on the use of these absorbers with precious metal HER catalysts. Here we present an alternative approach using a Sb_2Se_3/CdS/TiO_2-*meso* photocathode. The high surface area TiO_2 support, prepared by a UV and low temperature N_2 annealing process that is compatible with Sb_2Se_3, enables a high loading of an earth abundant molecular HER catalyst, **NiP**. An 81-fold increase in the photocurrent was achieved when compared to a similar device without the mesoporous TiO_2. Despite the high catalyst loading, stability and activity under 100 mW cm^{-2} is still limited by the turnover frequency of the HER catalyst. However, initial experiments under low light intensities indicate that improved stability is achievable with further advances in the catalytic turnover frequency.

We thank the studentship financial support from CONACYT-SENER (556479, DAGO), EPSRC (DTA, DAG), the UKRI Cambridge Creative Circular Plastics Centre (EP/S025308, ER, CC), and the European Commission for Horizon 2020 Marie Skłodowska-Curie Individual Fellowships (890745-SmArtC, CC). EPSRC is acknowledged for funding though EP/P034497/1, EP/N014057/1 and EP/V011863/1. Prof L. Hardwick and Facility for XPS (''HarwellXPS'') are thanked for the Raman spectroscopy access and the XPS data collection (Contract No. PR16195).

Conflicts of interest

There are no conflicts to declare.

Notes and references

1 S. Ye, C. Ding, R. Chen, F. Fan, P. Fu, H. Yin, X. Wang, Z. Wang, P. Du and C. Li, *J. Am. Chem. Soc.*, 2018, **140**, 3250–3256.
2 S. Ye, C. Ding, M. Liu, A. Wang, Q. Huang and C. Li, *Adv. Mater.*, 2019, **31**, 1902069.
3 H. Song, S. Luo, H. Huang, B. Deng and J. Ye, *ACS Energy Lett.*, 2022, **7**, 1043–1065.
4 R. M. Irfan, D. Jiang, Z. Sun, L. Zhang, S. Cui and P. Du, *J. Catal.*, 2017, **353**, 274–285.
5 S. Ye, W. Shi, Y. Liu, D. Li, H. Yin, H. Chi, Y. Luo, N. Ta, F. Fan, X. Wang and C. Li, *J. Am. Chem. Soc.*, 2021, **143**, 12499–12508.
6 H. Shiel, O. S. Hutter, L. J. Phillips, J. E. N. Swallow, L. A. H. Jones, T. J. Featherstone, M. J. Smiles, P. K. Thakur, T. L. Lee, V. R. Dhanak, J. D. Major and T. D. Veal, *ACS Appl. Energy Mater.*, 2020, **3**, 11617–11626.
7 O. S. Hutter, L. J. Phillips, K. Durose and J. D. Major, *Sol. Energy Mater. Sol. Cells*, 2018, **188**, 177–181.
8 A. Mavlonov, T. Razykov, F. Raziq, J. Gan, J. Chantana, Y. Kawano, T. Nishimura, H. Wei, A. Zakutayev, T. Minemoto, X. Zu, S. Li and L. Qiao, *Sol. Energy*, 2020, **201**, 227–246.
9 S. Chen, T. Liu, Z. Zheng, M. Ishaq, G. Liang, P. Fan, T. Chen and J. Tang, *J. Energy Chem.*, 2022, **67**, 508–523.
10 B. A. Pinaud, J. D. Benck, L. C. Seitz, A. J. Forman, Z. Chen, T. G. Deutsch, B. D. James, K. N. Baum, G. N. Baum, S. Ardo, H. Wang, E. Miller and T. F. Jaramillo, *Energy Environ. Sci.*, 2013, **6**, 1983–2002.
11 W. Yang, J. Park, H.-C. C. Kwon, O. S. Hutter, L. J. Phillips, J. Tan, H. Lee, J. Lee, S. D. Tilley, J. D. Major and J. Moon, *Energy Environ. Sci.*, 2020, **13**, 4362–4370.
12 W. Yang, J. H. Kim, O. S. Hutter, L. J. Phillips, J. Tan, J. Park, H. Lee, J. D. Major, J. S. Lee and J. Moon, *Nat. Commun.*, 2020, **11**, 1–10.
13 J. Tan, W. Yang, Y. Oh, H. Lee, J. Park, R. Boppella, J. Kim and J. Moon, *Adv. Energy Mater.*, 2019, 1900179.
14 J. Park, W. Yang, J. Tan, H. Lee, J. W. Yun, S. G. Shim, Y. S. Park and J. Moon, *ACS Energy Lett.*, 2020, **5**, 136–145.
15 W. Yang, S. Lee, H.-C. Kwon, J. Tan, H. Lee, J. Park, Y. Oh, H. Choi and J. Moon, *ACS Nano*, 2018, **12**, 11088–11097.
16 R. R. Prabhakar, W. Septina, S. Siol, T. Moehl, R. Wick-Joliat and S. D. Tilley, *J. Mater. Chem. A*, 2017, **5**, 23139–23145.
17 F. Niu, D. Wang, F. Li, Y. Liu, S. Shen and T. J. Meyer, *Adv. Energy Mater.*, 2019, 1900399.
18 W. Jiang, X. Yang, F. Li, Q. Zhang, S. Li, H. Tong, Y. Jiang and L. Xia, *Chem. Commun.*, 2019, **55**, 1414–1417.
19 M. L. Helm, M. P. Stewart, R. M. Bullock, M. R. DuBois and D. L. DuBois, *Science*, 2011, **333**, 863–866.
20 W. J. Shaw, M. L. Helm and D. L. du Bois, *Biochim. Biophys. Acta, Bioenerg.*, 2013, **1827**, 1123–1139.
21 M. A. Gross, A. Reynal, J. R. Durrant and E. Reisner, *J. Am. Chem. Soc.*, 2014, **136**, 356–366.
22 A. Paracchino, V. Laporte, K. Sivula, M. Grätzel and E. Thimsen, *Nat. Mater.*, 2011, **10**, 456–461.
23 T. E. Rosser, T. Hisatomi, S. Sun, D. Antón-García, T. Minegishi, E. Reisner and K. Domen, *Chem. – Eur. J.*, 2018, **24**, 18393–18397.
24 J. J. Leung, J. Warnan, D. H. Nam, J. Z. Zhang, J. Willkomm and E. Reisner, *Chem. Sci.*, 2017, **8**, 5172–5180.
25 T. E. Rosser, M. A. Gross, Y. H. Lai and E. Reisner, *Chem. Sci.*, 2016, **7**, 4024–4035.
26 T. Berger, D. Monllor-Satoca, M. Jankulovska, T. Lana-Villarreal and R. Gomez, *ChemPhysChem*, 2012, **13**, 2824–2875.
27 M. Schreier, J. Luo, P. Gao, T. Moehl, M. T. Mayer and M. Grätzel, *J. Am. Chem. Soc.*, 2016, **138**, 1938–1946.
28 NIST X-ray Photoelectron Spectroscopy (XPS) Database, Version 3.5, **https://srdata.nist.gov/xps/**, accessed 26 July 2022.
29 K. L. Materna, R. H. Crabtree and G. W. Brudvig, *Chem. Soc. Rev.*, 2017, **46**, 6099–6110.
30 A. Ruff, S. Janke, J. Szczesny, S. Alsaoub, I. Ruff, W. Lubitz and W. Schuhmann, *ACS Appl. Energy Mater.*, 2019, **2**, 2921–2929.